



Spray Coating Experiments: Setups and Methodologies



**The latest eBook from
Advanced Optical Metrology.
Download for free.**

Spray Coating Experiments: Setups and Methodologies, is the third in our Thin Films eBook series. This publication provides an introduction to spray coating, three article digests from Wiley Online Library and the latest news about Evident's Image of the Year Award 2022.

Wiley in collaboration with Evident, are committed to bridging the gap between fundamental research and industrial applications in the field of optical metrology. We strive to do this by collecting and organizing existing information, making it more accessible and useful for researchers and practitioners alike.

EVIDENT
OLYMPUS

WILEY

Nanogap Plasmonic Structures Fabricated by Switchable Capillary-Force Driven Self-Assembly for Localized Sensing of Anticancer Medicines with Microfluidic SERS

Zhaoxin Lao, Yuanyuan Zheng, Yichuan Dai, Yanlei Hu,* Jincheng Ni, Shengyun Ji, Ze Cai, Zachary J. Smith, Jiawen Li, Li Zhang, Dong Wu,* and Jiaru Chu

Nanogap plasmonic structures, which can strongly enhance electromagnetic fields, enable widespread applications in surface-enhanced Raman spectroscopy (SERS) sensing. Although the directed self-assembly strategy has been adopted for the fabrication of micro/nanostructures on open surfaces, fabrication of nanogap plasmonic structures on complex substrates or at designated locations still remains a grand challenge. Here, a switchable self-assembly method is developed to manufacture 3D nanogap plasmonic structures by combining supercritical drying and capillary-force driven self-assembly (CFSA) of micropillars fabricated by laser printing. The polymer pillars can stay upright during solvent development via supercritical drying, and then can form the nanogap after metal coating and subsequent CFSA. Due to the excellent flexibility of this method, diverse patterned plasmonic nanogap structures can be fabricated on planar or nonplanar substrates for SERS. The measured SERS signals of different patterned nanogaps in fluidic environment show a maximum enhancement factor $\approx 8 \times 10^7$. Such nanostructures in microchannels also allow localized sensing for anticancer drugs (doxorubicin). Resulting from the marriage of top-down and self-assembly techniques, this method provides a facile, effective, and controllable approach for creating nanogap enabled SERS devices in fluidic channels, and hence can advance applications in precision medicine.

1. Introduction

Nanogap plasmonic structures have the ability to enhance electromagnetic fields,^[1] consequently resulting in the development of a wide range of applications for such structures, including biological diagnosis and chemical sensing.^[2] As one of the most important applications, surface-enhanced Raman spectroscopy (SERS) offers a label-free and highly sensitive analytical technique by employing coupled nanogap structures for chemical molecule identification.^[3] In particular, SERS combined with microfluidic lab-on-a-chip (LoC) systems for sensitive optofluidic detection has spurred considerable interest over the past decade due to the intriguing advantages of real-time monitoring, ease of integration, and reusability.^[4] Furthermore, compared with ordinary SERS, microfluidic SERS devices can also provide a higher reproducibility profiting from effectively dissipating heat, removing analyte molecules damaged by high-power electric fields and averaging collected signals in a microfluidic environment.^[5]


Microfluidic systems that can generate drug-loaded microcapsules or other composite drug carriers are very useful in precision medicine, but there is a lack of effective monitoring of the packaged cargo.^[4b,6] Thus, fabricating localized SERS structures, which are designable at the single hot-spot level to minimize the effect on the microfluidic flow, would enable an in situ sensing of the concentrations and composition of a target drug solution within a microchannel.

The most critical issue for widespread and facile use of microfluidic SERS devices is how to construct SERS substrates in microchannels. Traditionally, nanogap plasmonic structures are fabricated by top-down approaches, for example, electron-beam lithography (EBL) or focused-ion-beam (FIB). However, it is always costly and time-consuming using EBL and FIB to fabricate such nanogap structures. In addition, fabricating smaller (e.g., sub-2 nm) plasmonic gaps, which enable greater electromagnetic enhancement,^[7] exceeds the manufacturing capacity of almost all single top-down strategies. As a significant complement to traditional nanofabrication approaches,

Dr. Z. Lao, Y. Dai, Prof. Y. Hu, Dr. J. Ni, S. Ji, Z. Cai, Prof. Z. J. Smith, Prof. J. Li, Prof. D. Wu, Prof. J. Chu
CAS Key Laboratory of Mechanical Behavior and Design of Materials
Key Laboratory of Precision Scientific Instrumentation of Anhui Higher Education Institutes
Department of Precision Machinery and Precision Instrumentation
University of Science and Technology of China
Hefei, Anhui 230027, China
E-mail: huyl@ustc.edu.cn; dongwu@ustc.edu.cn

Dr. Z. Lao, Prof. L. Zhang
Advanced Nanomaterials and Microrobotics Laboratory
Department of Mechanical and Automation Engineering
The Chinese University of Hong Kong
Shatin, New Territories 999077, Hong Kong

Dr. Y. Zheng
Institutes of Physical Science and Information Technology
Anhui University
Hefei 230601, Anhui, China

 The ORCID identification number(s) for the author(s) of this article can be found under <https://doi.org/10.1002/adfm.201909467>.

DOI: 10.1002/adfm.201909467

bottom-up strategies have been widely studied by exploring molecular interaction, electrostatic force, or other weak forces to assemble nanostructures. Self-assembly of nanoparticles (NPs) has been also introduced for the fabrication of nanogap enabled plasmonic structures.^[14] Yet, NPs self-assembly for microfluidic SERS suffers from relatively low controllability due to its random nature.^[2c,8] To integrate the merits of both approaches, meanwhile eliminating the respective shortcomings, bottom-up self-assembly has been combined with conventional top-down processes to manufacture complex 3D micro/nano functional structures.^[9] For instance, capillary-force self-assembly (CFSA) has been combined with other top-down strategies (e.g., UV-lithography, EBL, nanoimprinting, and FIB) to fabricate 3D complex nanostructures with high precision and controllability.^[10] However, inherent disadvantages (e.g., inflexibility, multi-step fabrication, time-consuming, and high cost) of these top-down methods hinder their applications in constructing nanogap plasmonic structures for SERS. Especially, these top-down methods lack the ability to integrate nanostructures in microfluidic channels with non-planar substrates for SERS in LoC systems. Some creative methods have been proposed to integrate SERS nanostructures within a microfluidic chip by electron beam,^[11] soft lithography,^[12] liquid printing,^[13] and laser direct writing,^[14] so that Ag flowers/columns can be fabricated in channels for microfluidic SERS application. However, these discoid alloys are more suitable for large-areas manufacture rather than localized sensing in some situations, for example, microfluidic packaging system.^[15] Besides, such strategies may lack sufficient positioning accuracy to integrate microflowers/micropillars at designated locations in small or complex channels and lack favorable controllability to adjust properties of single SERS nanostructures within a measuring laser focus.^[16] Therefore, flexible and localized integration of SERS nanostructures inside a microfluidic chip still remains a challenge.^[17] Laser printing based on two-photon-polymerization (TPP), which possesses the unique advantages of simple integration, mask-free processing, and suitability for nonplanar substrates, is an excellent candidate for fabricating 3D micro/nano structures.^[18] By combining laser printing with CFSA, complex hierarchical micro/nano structures can be expediently constructed.^[19] Nonetheless, till now, only photopolymer materials can be printed by TPP, which can hardly be utilized to form plasmonic nanogaps for electromagnetic enhancement.^[19b,20]

Here, a switchable CFSA method is developed to realize nanogap plasmonic structures in microchannels by combining supercritical drying, metal sputtering, and capillary-force driven self-assembly (CFSA) of micropillars fabricated by laser printing. Firstly, a supercritical drying method was used to avoid the CFSA of the polymer pillars and keep the pillars upright during solvent development. After coating a functional Au nanofilm on the pillars, the CFSA is used to bend the pillars together and construct metal nanogap structures which results in the plasmonic hotspot. As a proof-of-concept demonstration, SERS experiments in a liquid environment are performed to sense Rhodamine-6G (R6G). Besides, doxorubicin (DOX), a widely used anticancer drug, was also measured. The effect of diverse patterned nanogaps for sensing R6G and DOX is studied via both simulation and

experiment. Finally, the dependence on analyte concentration and the repeatability are also characterized. These results demonstrate that such SERS structures, which can be integrated in microchannels, will be an important alternative strategy to current fabrication methods of SERS structures and will have great potential in the area chemical analysis and biological sensing.

2. Result and Discussion

2.1. Assembled Nanogap Structures Fabricated by Switchable CFSA

The strategy to fabricate the self-assembled metal nanogap structure is schematically presented in **Figure 1a**. Firstly, by focusing a femtosecond laser beam into a commercial photoresist, polymer pillars were fabricated on a glass slide by a typical 3D laser printing process. The sample was placed on a 3D nanotranslation stage so that the parameters (e.g., location and height) of structures could be flexibly regulated. Following the laser printing, the sample was put into n-propanol in the developing process to remove the unpolymerized photoresist. However, if dried under normal conditions, the polymer pillars will be attracted toward each other by CFSA. To prevent this, after taking structures from the developing liquid, we introduced a supercritical drying method to switch the capillary force (F_c) so that the polymer pillar can remain upright before CFSA. Then, in order to build the noble metal nanogap, the polymer pillar was coated with a gold (Au) nanofilm, which will make the polymer pillar into a polymer-metal compound structure. After immersing the sample into solvent, the polymer-metal compound pillars bend together by CFSA to form metal nanogap. **Figure 1b** shows an optical image of as-prepared upright polymer pillars. Without the switch, the high-aspect-ratio (HAR) polymer pillars would collapse to leaning structures which, when coated with gold, would not form a nanogap plasmonic structure. Then, the Au nanofilm was coated onto the upright polymer pillars by using an ion sputtering system as shown in **Figure 1c**. The thickness of the Au nanofilm can be tuned via adjusting coating time and coating electric current (**Figure S1**, Supporting Information). After coating the functional Au nanofilm, a droplet of water was dropped on the structures so that a meniscus will arise during the evaporation of liquid. As the F_c in this case is larger than the restoring standing force (F_s) of Au-polymer compound pillars, periodic hierarchical architectures were constructed. **Figure 1d** shows homogeneous assembled 6-pillar structures with ≈ 850 nm diameter, 18 μm height, 3.5 μm distance, and coated 10 nm thickness Au film. SEM image in **Figure 1e** demonstrates the magnified nanogap structures corresponding to the structure in **Figure 1d**. Furthermore, inheriting the powerful tunability of fs-laser printing, the shape, size, and spatial distribution of pillars can be easily controlled for the generation of diverse ordered patterns at any desired position. As an evidence of the high flexibility, more intricate “NANOGAP” and “Taiji” patterns formed by nanogap structures assembled with 4-pillars are also realized and presented in **Figures 1f,g**.

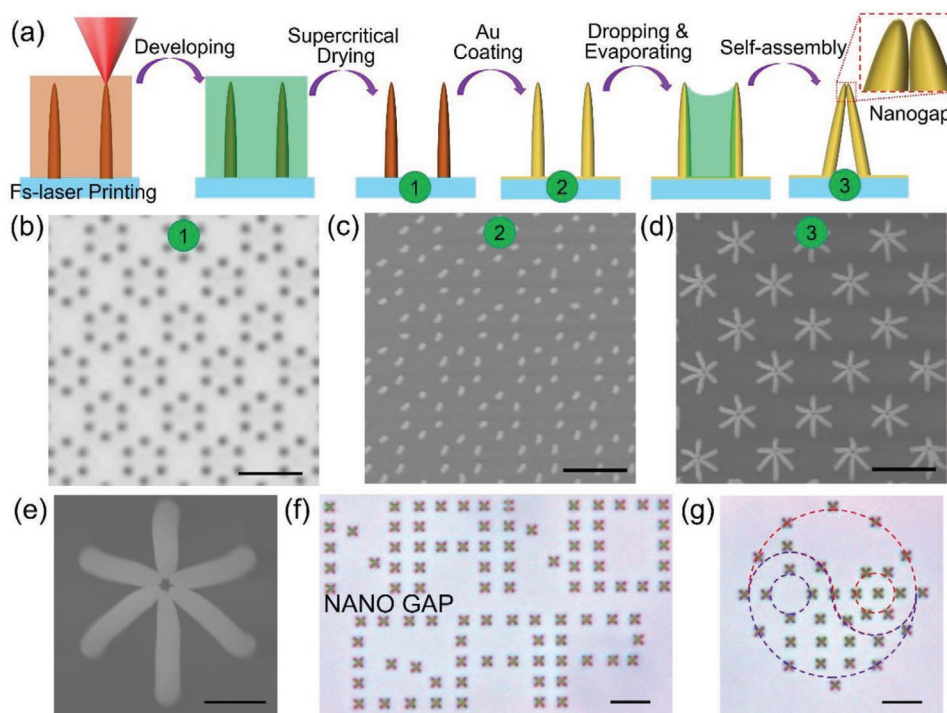


Figure 1. Fabrication of nanogap enabled plasmonic structures with supercritical drying-switchable capillary-force self-assembly (CFSA). a) Firstly, the polymer pillars were fabricated with a typical laser printing and developing process. Then, a supercritical drying method was employed to switch the capillary force, without which the pillars would collapse before coating. Noble metal was coated on the pillars as functional film. Finally, the nanogap can be formed after the CFSA of the coated pillars. b) Optical image of upright polymer pillars before coating. SEM image of coated pillars with 10 nm Au film before self-assembly (c) and self-assembled structures with nanogaps (d). e) Enlarged image of patterned nanogap structure in (d). f,g) The optical images of a “nanogap” and a “Taiji” pattern formed with 4-pillar nanogap structures. Scale bars: b–d) 10 μm ; e) 2 μm ; f,g) 20 μm .

2.2. Switchable CFSA Affected by Au Coating and Supercritical Drying

Though using noble metal-coated polymer pillars to fabricate nanogap enabled SERS structures has been reported previously,^[19,20] these prior works utilize fabrication strategies that cannot be straight forwardly adapted to in-channel environments, and furthermore there is still a lack of detailed analysis about how the polymer-metal compound structures affect CFSA compared with a simple polymer pillar. There are two main forces involved in self-assembly of micropillars: the F_c caused by the meniscus of liquid and F_s of microstructures. F_c can be considered as

$$F_c \approx \gamma r^2 \cos^2 \theta \cdot \frac{\Delta d}{d(d + \Delta d)} \quad (1)$$

Here, γ , r , θ , d , and Δd represent the interfacial tension of the solvent, the radius of the pillars, contact angle, the spacing distance between adjacent pillars, and additional spacing between two adjacent units, respectively. The CFSA among this plasmonic micropillars was initiated by introducing a small water droplet onto the structures to conquer F_s (Figure S2, Supporting Information). The F_s of structures can be described as

$$F_s \approx \frac{Er^4 d}{h^3} \quad (2)$$

where E is Young's modulus; r and h are the radius and height of the pillars; d is the collapse distance for assembly. Compared with polymer pillars, the F_s of compound pillar after coating will enlarge for the following two reasons: First, the E of Au film is larger than that for polymers. Second, the circular cross section, which changes the cross-sectional moment of inertia, enlarges as a result of the Au coating. Therefore, F_s would enlarge after the coating process. In order to make F_c larger than the F_s of compound structures, the height of the pillars are designed to be three times larger than our previous work, which results in a smaller F_s leading to an easier collapse of polymer pillars when it was taken from the liquid developer before coating (detailed discussion can be seen in the Supporting Information). Therefore, we introduced the supercritical drying method as a switch into CFSA so that detached upright polymer pillars can be obtained prior to coating the plasmonic functional material.

Due to the fact that the different structure of polymer pillars and metal-polymer pillars will result in different F_s , it is worth analyzing how the metal coating film will affect the standing force. Figure 2a,b shows the vertical and horizontal profile of a typical metal coated polymer pillar. According to formula 2, when the h of pillar and the d are fixed,

$$F_s \approx ED^4 \quad (3)$$

where D is the diameter of a pillar. A thicker Au film means a larger F_s , which will make coated pillars harder to assemble

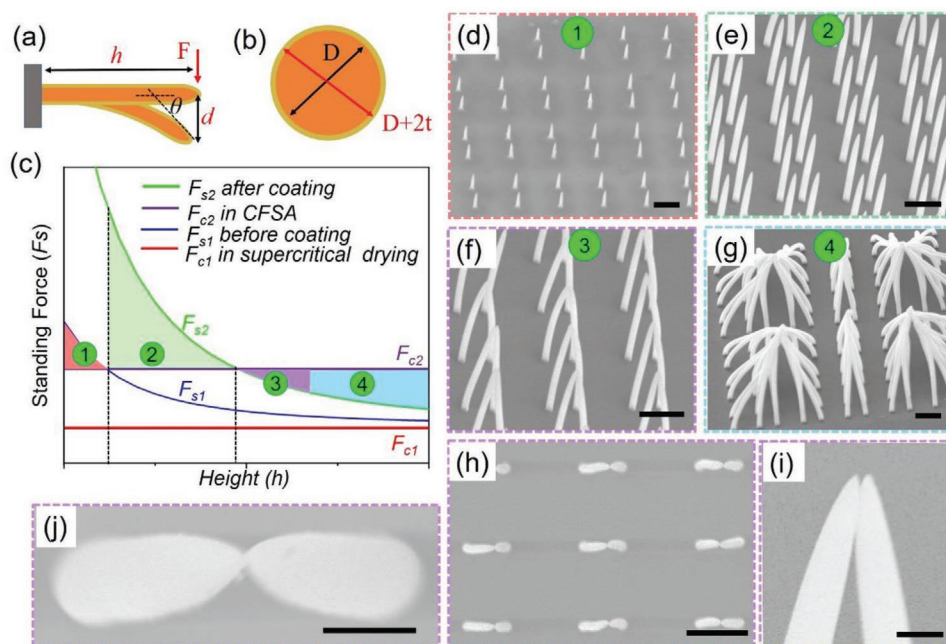


Figure 2. The influence of coated Au nanofilm and pillar parameters on CFSA. a,b) Illustration of the metal-polymer compound pillars. c) The schematic diagram of different dependence on microstructure parameters of compound and polymer pillars. d–g) Assembled result corresponding to different areas in (c). d) When the height is too small, capillary force too small to conquer standing force without coating ($F_{c2} < F_{s1}$). Pillars cannot assemble. (Zone 1). e) When the height enlarges, capillary force is smaller than the standing force after coating ($F_{c2} < F_{s2}$). Pillars with coating cannot assemble. (Zone 2); f) compound pillars with suitable height will assemble to form a patterned nanogap, corresponding to zone 3 in (c). g) When the height is too large, capillary force is so big that ($F_{c2} > F_{s2}$) pillars collapse to unordered structures. (Zone 4). h–j) The top and tilted views of the assembled compound pillars with a suitable height. Scale bars: d–h) 5 μm ; g) 1 μm ; i,j) 500 nm.

unless we enlarge the height of the pillars. Considering that extreme thickness of Au easily results in difficult collapse of pillars after coating, Au thickness in experiment was set at 10 nm. The standing force (F_{s2}) of metal-polymer compound pillar after coating is ≈ 10 times larger than the standing force (F_{s1}) of polymer pillar (detailed discussion can be seen in the Supporting Information). To simplify the discussion, we studied how to regulate F_c and F_s in this switchable CFSA via changing height (h) by assuming the parameters of pillars are fixed except h . Noticing that the upright pillars collapse into patterns as the result of competition between F_c and F_s , there are four forces involved in this discussion: the standing force of pillars before (F_{s1}) and after (F_{s2}) coating, the capillary force during (F_{c1}) and without (F_{c2}) supercritical drying process. As shown in Figure 2c, F_s evolves with the change of h while F_c remains constant because other parameters are fixed, which means that the evolution map can be divided into four parts with increasing h . When h is very small, F_{s1} is so large that it is bigger than F_{c1} , resulting in upright polymer pillars (area 1 and Figure 2d). In area 2, because of the increase in h , F_s is weakened but still larger than F_{c2} after coating ($F_{s2} > F_{c2}$), leading to upright metal-polymer compound pillars (Figure 2e). However, if h is too large, F_s will badly decrease ($F_{s2} \ll F_{c2}$) so that unordered structures are formed (Figure 2g). Only in the situation that $F_{s1} > F_{c1}$ and $F_{s2} < F_{c2}$ can this nanogap enabled plasmonic structure be realized (area 3 in Figure 2c, Figure S4, Supporting Information). Figure 2f–h shows the tilted and top view of this assembled structure, while Figure 2i,j displays magnified nanogap structures fabricated with this switchable CFSA.

Although we only discuss how h affects assembly here, the exposure dose can also be controlled to obtain structures with tunable diameters and elasticity, which contributes to different assembly configurations benefiting from the tunability of the laser printing method. After assembly, what resists F_s to hold the structures in their assembled configuration is the Van der Waals' force (F_v) that appears when the tops of micropillars are in contact. After re-immersion in liquid, F_s would tend to make the assembled structures return to their initial upright position. This force is counteracted by the F_v . According to formula 2, the bigger the height is, the smaller the F_s is, allowing it to be more easily counterbalanced by F_v and, therefore, the nanogap structures can keep their configuration after assembly even when they are immersed in liquid again, which is important for microfluidic applications.

2.3. Nanogap Enabled SERS Structures Integrated in Microchannel

Because of prominent flexibility of this switchable CFSA, nanogap enabled plasmonic microstructures can be fabricated not only on flat substrates but also in micro channels. The schematic of laser printing inside microfluidic channels is shown in Figure 3a. Patterned nanogap structures in channels formed by 6-pillar units are shown in Figure 3b,c, which possess different rotations and high repeatability. According to the previous research,^[9c] when the assembled structures in liquid were immersed again, liquid molecules would invade into the

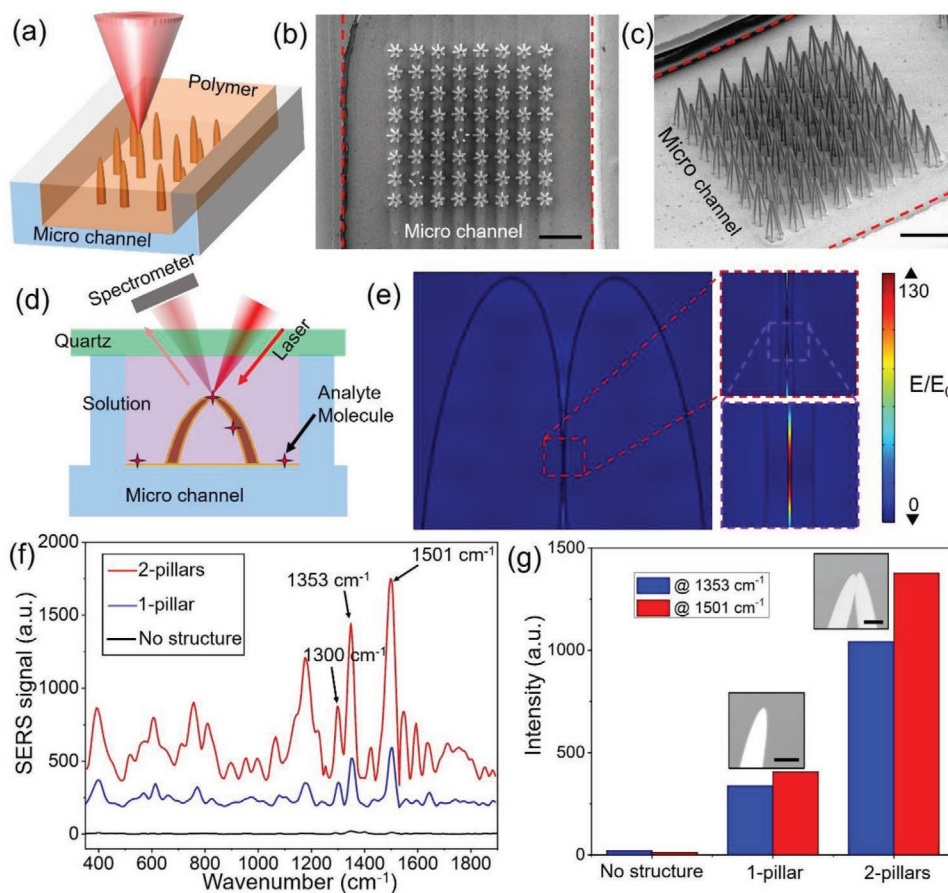


Figure 3. Nanogap enabled microfluidic SERS device integrated in microchannels. a) The fabrication illustration of microstructures in channels. b,c) Top view and tilted view, respectively, of nanogap plasmonic structures fabricated with the switchable CFSA method. d) Schematic diagram of self-assembled nanogap structure in channel used for microfluidic SERS device. e) Simulation of the enhancement in the nanogap between 2-pillars. The thickness of Au is 10 nm and the gap is 2 nm. A circularly polarized laser (785 nm) is used as the excitation light. The maximal E/E_0 is about 130. f) The SERS signal of different structures in microfluidic channels which present an obvious enhancement of the Raman signal of the 2-pillars with a nanogap. g) Normalized intensity of signals in (f) at 1353 cm^{-1} and 1501 cm^{-1} . Inset images show 1-pillar and 2-pillar nanogaps, respectively. Scale bars: b,c) $20\text{ }\mu\text{m}$; g) $1\text{ }\mu\text{m}$.

nanogap between the assembled structures so that probe molecules would enter the nanoscale gap. Therefore, this nanogap structure in a microfluidic channel demonstrates the application of SERS sensing (Figure 3d). Corresponding to prior literatures and our own simulations, the polarization of the laser and symmetry of the structures would obviously affect the enhancement of the electromagnetic field (Figures S5 and S6, Supporting Information). To erase the difference of SERS caused by electrical polarization between different structures with asymmetry, here we employed a circularly polarized laser to excite SERS, in which the enhancement factor of SERS is related to the number of nanogaps and the plasmonic enhancement of a single nanogap. As mentioned above, when the assembled structures were immersed in liquid again, both liquid and analyte molecule would invade into the assembled area. Therefore, to quantitatively discuss our expected results, we evaluated the nanoscale gaps to be less than 5 nm in the simulations. The simulation in Figure 3e demonstrates the enhancement of these plasmonic structures, in which E/E_0 is inversely related to the gap size and can be enlarged to as much as 130 when the gap is 2 nm (Figure S5, Supporting Information).

Here, rhodamine 6G (R6G), a common compound used in SERS characterization studies due to its well-established vibrational features, was adopted as the probe molecule to evaluate the SERS performance of the patterned nanogap substrates. In order to acquire the SERS signals, a home-built Raman spectroscopy system whose excitation wavelength is 785 nm was utilized. The acquisition time for SERS signal collection was set at 1 s with 3 mW of exciting laser power. To evaluate the nanogap enabled microfluidic SERS device, Raman spectra of 1 mM R6G molecule adsorbed on different structures is presented in Figure 3f. Typical R6G signals can be received on 1-pillar and 2-pillars nanogap structures, while there is no obvious signal on the metal coated substrate without the structure. Note that the tip of 1-pillar structures can also provide a distinct SERS spectra because of nanoscale tip and Au particles on pillars (inset of Figure 3g), which have a great impact on electromagnetic enhancement. As shown in Figure 3g, the normalized intensity of SERS signals of nanogaps formed by 2-pillars is about four times larger than the signal of 1-pillar structures at both 1353 cm^{-1} and 1501 cm^{-1} peaks, verifying that the nanogap substantially contributes to the SERS spectra.

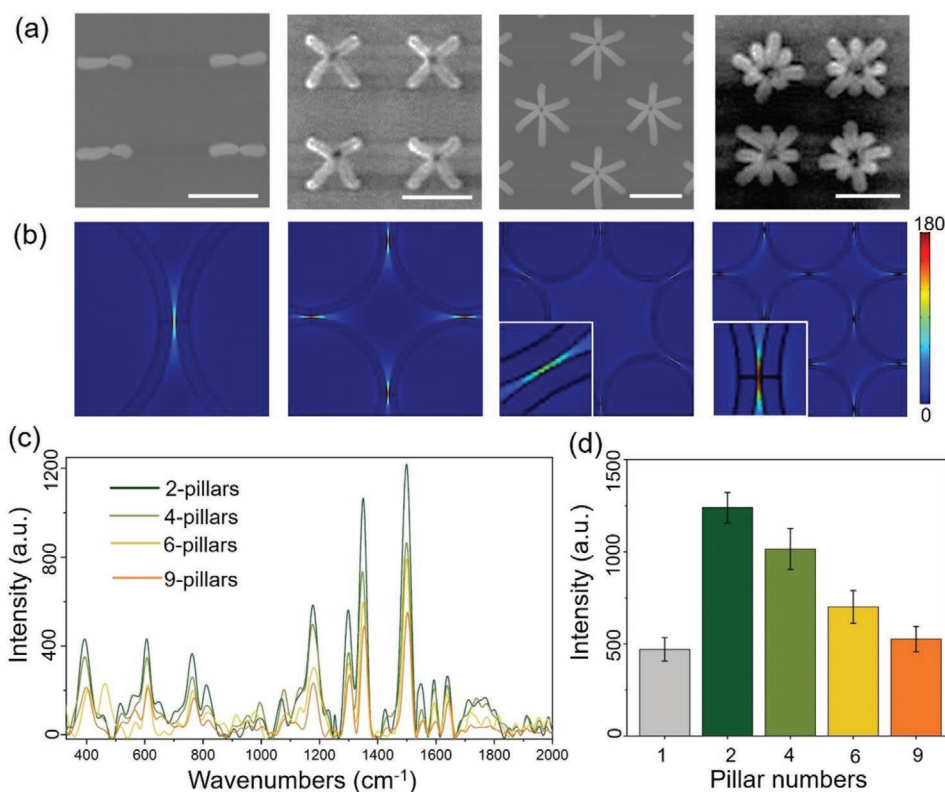


Figure 4. The SERS sensing of different nanogap patterns. a,b) SEM images and corresponding simulations of enhanced electromagnetic fields of different patterned nanogap structures. In the simulation, the thickness of the Au film is 2 nm, the gap is 2 nm, the irradiating laser is 785 nm, and is circularly polarized. c) Comparison of intensity at 1501 cm^{-1} with different patterned nanogaps. The result shows that the 2-pillar nanogap possesses the maximal signal for R6G in a microfluidic environment for 785 nm incident radiation. The intensity decreases while pillars in the pattern increase, which may be due to the fact that the more numerous are the pillars, the more difficult it is for the pattern to assemble into a smaller gap. d) R6G excited SERS signals of different nanogap patterns. Excitation laser, 785 nm, 3 mW, circular polarization; integration time, 1 s. All scale bars: 5 μm .

In order to evaluate the sensing ability of nanogap enabled SERS structures, the enhancement factor (EF) was calculated according to the following formula

$$EF = \frac{I_{\text{SERS}} \times N_{\text{bulk}}}{N_{\text{SERS}} \times I_{\text{bulk}}} \quad (4)$$

where I_{SERS} is the intensity of a vibrational mode in the surface enhanced Raman spectrum; I_{bulk} is the intensity of the same mode in the Raman spectrum; N_{SERS} is the number of molecules adsorbed on the alloy substrate within the laser spot area, and N_{bulk} is the number of molecules excited by the laser focus in a bulk sample that contributes to the SERS signals. According to the experimental results, the EF value of the 2-pillar nanogap enabled SERS microfluidic structure was calculated to be about 8×10^7 (detailed calculation can be seen in the Supporting Information).

2.4. SERS Signals of Different Patterned Nanogap Structures

We investigated how the nanogap pattern affects the SERS sensing. Different nanogap patterns assembled by 2-, 4-, 6-, and 9-pillars were manufactured ascribing to the flexibility of our switchable CFSA strategy. Figure 4a shows SEM images of

different nanogap structures. In order to analyze the signals, the simulations of electronic fields enhanced by different patterned structures were carried out and are correspondingly shown in Figure 4b. Considering that the plasmonic gap only works in a very small area (≈ 2 nm) while the length of pillar is 10 000 times larger (≈ 20 μm), in order to simplify the simulation, we built a similar model to present the polymer pillar coating with Au nanofilm. In the simulation, Au film was set at 10 nm; the nanogap between pillars was set to 2 nm. Simulation predicts that the gap in different patterned structures possess different maximum electromagnetic enhancement (E/E_0), which varies from 180 to 50, when the gaps were irradiated by 785 nm with circular polarization. Owing to the circularly polarized laser, we can find that enhanced field has symmetric distribution due to the symmetry of assembled structures in different patterns (Figure 4b). Therefore, we can speculate that electromagnetic enhancement depends on the size and valid number of gaps for different patterns in the case of irradiating with a circular polarization. The simulation shows that enhancement factor should increase while pillars in the pattern increase if the sizes of nanogap are equal. Subsequently, R6G ethanol solution was tested in microfluidic SERS device. The Raman spectra of R6G excited by 785 nm laser on 2-, 4-, 6-, and 9-pillars nanogap arrays indicates that all structures generated similar SERS spectral line shapes, suggesting that there is no significant

difference in terms of the enhancement mechanism from the various symmetries of the pillar assemblies (Figure 4c).

The simulated maximum values of electronic field (E) of different pattern were performed by assuming the gaps same (2 nm), which indicates that single gap in 9-pillars pattern possesses E maximum (Figure S7a, Supporting Information). Considering E^4 and gap number in patterns, 9-pillars microstructures would achieve the strongest pattern sensing ability (Figure S7b, Supporting Information). However, the experimental results present that the intensity decreases as the number of pillars in the pattern increases and the 2-pillar nanogap possesses the maximum signal among five different patterns, which is different from the model simulation at the same gap size (Figure 4d). We hypothesize that this discrepancy is caused by the different gap sizes between assembled structures, because the nanogap structures are assembled by the upper area of pillars, which means that, as the assembled area is not a tip point, different patterns would result in different gap sizes (Figures S8 and S9, Supporting Information). Thus, as the number of pillars in the pattern becomes larger, it is more difficult for the assembled pattern to form smaller gaps (Figures S8 and S9, Supporting Information). The signal weakens with enlarging gap so sharply that this weakness cannot be made up by the increase of number of gaps and pillars. However, the experimental results of different patterns possess relatively small deviations among different pattern elements, proving that assembled structures of the same pattern have a consistent gap size when fabricated with this strategy.

2.5. Sensing Ability and Potential Application of Nanogap Enabled SERS Structures in Channel

Furthermore, the sensing capability of nanogap enabled microfluidic SERS structures for different analyte concentrations was also tested. While the concentrations of R6G ethanol solution varies from 10^{-3} to 10^{-6} M, typical Raman spectra of R6G are shown in Figure 5a. The average peak intensities at the 1501 cm^{-1} band (Figure 5b) indicates that the nanogap enabled SERS device possesses high sensitivity (10^{-6} to 10^{-3} M) for R6G sensing in microfluidic environments under the 785 nm irradiation. To detect the reproducibility of such nanogap enabled SERS structures in a microfluidic environment, SERS spectra of R6G solution (10^{-3} M) from ten different 2-pillar nanogaps were collected under identical experimental conditions (Figure 5c). These ten spectral traces are nearly the same, which suggests that the nanogap enabled SERS structures have good reproducibility.

One potential application of this SERS is the in situ detection of target drugs used in microfluidic encapsulation or biological reaction. Doxorubicin (DOX), as a DNA intercalating agent, is widely used in anticancer treatment and could effectively treat various types of cancers. Because of the cardiac and hematopoietic toxicity, the therapeutic dose is limited to ≈ 30 mg per injection so that the concentration of DOX applied for microfluidic packaging in many research ranges from sub- μM to few μM .^[21] Here, different concentrations of DOX in aqueous solution were tested, which demonstrates that the limit of detection is about 0.1 μM (Figure 5d,e). To investigate the effect of different

nanostructures on the SERS signals from DOX, Raman spectra of several structures with varying thicknesses of Au were tested, which presents that the SERS signals get bigger as the thickness of Au coating increases when the concentration of DOX is larger than 0.1 μM (Figure S12, Supporting Information). Similarly, Raman spectra of DOX (10^{-3} M) were taken at ten different 6-pillar nanogaps under identical experimental conditions (Figure 5f), illustrating that the Raman spectra show good reproducibility. Only slight fluctuations of the peak intensity at 1224 cm^{-1} could be observed, with a small relative standard deviation (RSD) of 8.1% (Figure 5f). Hence, this type of directly fabricated chip with a microfluidic SERS structure can provide repeatable and sensitive detection of drugs or other chemicals.

3. Conclusion

In summary, a CFSA strategy was developed to construct nanogap plasmonic structures, which show great potential for microfluidic SERS sensing. A supercritical drying method was adopted to switch the capillary force during CFSA so that the noble metal nanofilm can be evaporated as the functional coating. Due to the flexibility and 3D processing capability of laser printing, the nanogap enabled SERS microstructures can be developed both on planar substrates and in microchannels. Then, the sensing capability of this nanogap enabled SERS structures in microchannel was proved via SERS measurements of R6G. For different nanogap patterns, we find the structure formed by 2-pillars possesses the best response to a typical probe molecule (R6G) for SERS in a microfluidic environment. Besides, such structures also proved the ability to sense anticancer drug in channels, which presents the potential application for in situ monitoring in microfluidic packing system for the fabrication of microcapsules in precision medicine. Benefiting from laser printing combined with CFSA to construct nanogap enabled SERS structures in microchannels, although it is difficult to fabricate large-scale SERS substrates, this strategy will be an excellent supplement for the fabrication of microfluidic SERS devices and will find extensive applications in biological analysis and chemical sensing, for example, microfluidic packaging system used in the field of precision medicine.

4. Experimental Section

Laser Printing: A Ti:sapphire femtosecond laser system (Chameleon Vision-S, Coherent Inc., USA) was used for direct laser writing. The central wavelength, pulse width, and repetition rate of the laser source were 800 nm, 75 fs, and 80 MHz, respectively. A laser with energy varying from 55 to 70 mW was passed through a 50 \times objective lens (NA = 0.8; Olympus) to polymerize the material (SZ2080 photoresist, IESLFORTH, Greece). The energy was measured before entering the microscope. The laser power or curing time was tuned within the presented ranges to satisfy the appropriate parameters of the micropillars (diameter and Young's modulus). The sample was mounted on a nanopositioning stage (E545, from Physik Instrumente GmbH & Co. KG, Germany) with nanometer resolution and a $200\text{ }\mu\text{m} \times 200\text{ }\mu\text{m} \times 200\text{ }\mu\text{m}$ moving range to precisely locate microstructures. After being polymerized by a femtosecond laser, the sample was developed in 1-propanol for 30 min until all of the unpolymerized material was washed away. The

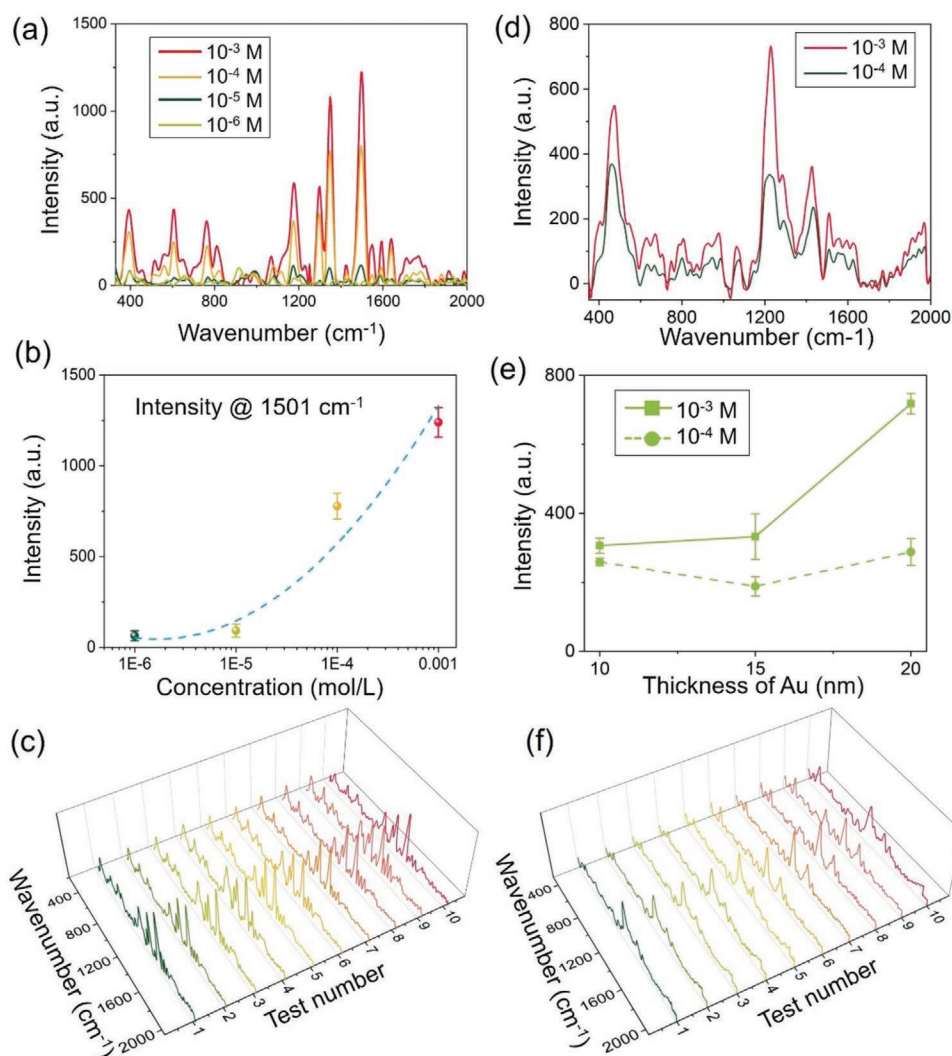


Figure 5. Localized sensing of R6G and anticancer medicines by nanogap enabled SERS structures in channel. a) Different Raman signals of R6G with different concentrations. b) Evolution of the signals at 1501 cm^{-1} for different concentrations. It indicates that, such prepared microfluidic SERS structures may achieve a detecting accuracy about $1\ \mu\text{M}$. c) SERS spectra of R6G collected on ten randomly selected 2-pillar structures. The RSD is about 6.6%. d) The Raman spectra of anticancer drugs (DOX) with different concentrations on self-assembled patterns with 20 nm coating. e) Evolution of the signals at 1224 cm^{-1} for the DOX with different concentrations, which demonstrates that the limit of detection is about $0.1\ \mu\text{M}$. f) SERS spectra of DOX ($1\ \mu\text{M}$) collected on ten randomly selected nanogap 6-pillar structures. The RSD is about 8.1%.

microchannels were fabricated with typical UV-lithography approach. SU-8 (2025, MicroChem, Suzhou Research Material Microtech, Suzhou, China) was spin coated onto the glass at 3000 rad min^{-1} for 20 s, so that the depth and width of SU-8 microchannels are $\approx 30\ \mu\text{m}$ and $\approx 90\ \mu\text{m}$, respectively.

Nanogap Structure Fabrication and Characterization: During the evaporation process after withdrawal from 1-propanol, the micropillar array was rapidly put into the supercritical drying instrument (Leica EM CPD300, Leica, Germany) to avoid the assembly driven by capillary forces. An ion sputtering system (AGAR Auto Sputter Coater, AGAR Scientific Technology, HongKong, China) was used for the Au coating. The sputter current setting was 30 mA, while the deposition speed of Au was about $0.14\ \text{nm s}^{-1}$. The SEM images were taken with a secondary electron scanning electron microscope (ZEISS EVO18) operating at an accelerating voltage of 10 keV after depositing $\approx 10\ \text{nm}$ of gold. An optical microscope (DMI 3000B, Leica) with a white light source performed bright-field imaging of the structures. By dropping a liquid on the sample ($\approx 20\ ^\circ\text{C}$ temperature), the Au-polymer compound pillars

could be assembled into diverse patterns if the capillary force of the liquid conquers the standing force of the pillars.

SERS Test: SERS spectral acquisition was performed on a homebuilt Raman spectroscopy system. The light source used was a 785 nm laser (Sacher PilotPC 4000) directed through a $40\times/0.95\ \text{NA}$ microscope objective lens (W Plan-Apochromat, Nikon, Japan) and brought to a diffraction limited spot ($\approx 1\ \mu\text{m}$ spot diameter) at the sample plane, with 3mW of laser power at the sample plane. The laser was filtered with a bandpass filter, and the Raman light was separated from the excitation light via a dichroic beamsplitter. Finally, the laser-line was further blocked with a long-pass filter. All filters were purchased from Semrock (Rochester, NY). The filtered Raman scattered light was collected via a $105\ \mu\text{m}$ fiber with a $150\ \text{groove mm}^{-1}$ grating spectrograph (Shamrock, Andor, UK) and spectra were acquired using a thermoelectrically cooled back-illuminated CCD camera (iDus DU401-DD, Andor, Belfast, UK) with a spectral resolution of $14.5\ \text{cm}^{-1}$ and a wide spectral range of $>3500\ \text{cm}^{-1}$. To manipulate the spatial position of the sample under the microscope, an open-loop control system was built with a step motor (Z812B) whose

step size is 0.03 μm in the X, Y, and Z direction. Rhodamine 6G (R6G; SCRC71036883, SCR Company, Shanghai, China) and doxorubicin (DOX; Solarbio, Beijing Solarbio Co., Ltd, Beijing, China) were chosen as the analytes in the SERS experiments. In the experiments, DI aqueous solution of R6G and DOX with different concentration surrounds the assembled metal-polymer compound structures in channels under the 785 nm excitation. The signals were packed up at the position with minimum self-assembled nanogap structures corresponding to a maximum intensity of SERS (Figure S12, Supporting Information).

Simulations: The simulations were carried out using COMSOL Multiphysics 5.3a. The metal-polymer compound nanogap structure was sketched directly in COMSOL, which has a similar profile of experimental results according to SEM images. A circularly polarized 785 nm plane wave illumination beam was directed onto the plasmonic nanostructures. The gap was set to 2 nm. The thickness and permittivity of gold was set to 10 nm and $\epsilon_{\text{Au}} = -22.855 + 1.425i$.^[20c] The permittivity of polymer (SZ2080) was defined as 1.5.

Supporting Information

Supporting Information is available from the Wiley Online Library or from the author.

Acknowledgements

This work was supported by the National Natural Science Foundation of China (Nos. 51805509, 91963127, 51875544, 61475149), the Fundamental Research Funds for the Central Universities (WK2090090012, WK2090090021), and Youth Innovation Promotion Association CAS (2017495). Z.L. thanks the funding of the Hong Kong Scholar Program (XJ2018035). The authors acknowledge the Experimental Center of Engineering and Material Sciences at USTC for the fabrication and measuring of samples. This work was partly carried out at the USTC Center for Micro and Nanoscale Research and Fabrication.

Conflict of Interest

The authors declare no conflict of interest.

Author Contributions

Z. L. and Y. Z. contributed equally to this work. Z.L., Y.H., and D.W. designed the experiment. Z.L., J.N., and Z.C. fabricated samples. Y.Z., Y.D., and Z.J.S. performed microfluidic experiments and SERS tests. Z.L. and S.J. conducted the simulations. Z.L. and Y.Z. analyzed the data and prepared the manuscript. Z.J.S., J.L., L.Z., and J.C. reviewed and revised the paper.

Keywords

laser printing, nanogaps, self-assembly, surface-enhanced Raman spectroscopy

Received: November 12, 2019

Revised: January 17, 2020

Published online: February 20, 2020

- [1] a) J. A. Fan, C. Wu, K. Bao, J. Bao, R. Bardhan, N. J. Halas, V. N. Manoharan, P. Nordlander, G. Shvets, F. Capasso, *Science* **2010**, 328, 1135; b) J. A. Schuller, E. S. Barnard, W. Cai, Y. C. Jun,

- J. S. White, M. L. Brongersma, *Nat. Mater.* **2010**, 9, 193; c) X. Chen, C. Ciraci, D. R. Smith, S. H. Oh, *Nano Lett.* **2015**, 15, 107; d) D. Yoo, N. C. Nguyen, L. Martin-Moreno, D. A. Mohr, S. Carretero-Palacios, J. Shaver, J. Paire, T. W. Ebbesen, S. H. Oh, *Nano Lett.* **2016**, 16, 2040; e) S. Zhang, G.-C. Li, Y. Chen, X. Zhu, S.-D. Liu, D. Y. Lei, H. G. Duan, *ACS Nano* **2016**, 10, 11105.
- [2] a) P. G. Etchegoin, E. C. Le Ru, *Phys. Chem. Chem. Phys.* **2008**, 10, 6079; b) E. Petryayeva, U. J. Krull, *Anal. Chim. Acta* **2011**, 706, 8; c) N. Pazos-Pérez, W. Ni, A. Schweikart, R. A. Alvarez-Puebla, A. Fery, L. M. Liz-Marzán, *Chem. Sci.* **2010**, 1, 174; d) Q. Jin, M. Li, B. Polat, S. K. Paidi, A. Dai, A. Zhang, J. V. Pagaduan, I. Barman, D. H. Gracias, *Angew. Chem., Int. Ed.* **2017**, 56, 3822.
- [3] a) A. Kim, S. J. Barcelo, R. S. Williams, Z. Li, *Anal. Chem.* **2012**, 84, 9303; b) D. Lin, Z. Wu, S. Li, W. Zhao, C. Ma, J. Wang, Z. Jiang, Z. Zhong, Y. Zheng, X. Yang, *ACS Nano* **2017**, 11, 1478.
- [4] a) J.-A. Huang, Y.-L. Zhang, H. Ding, H.-B. Sun, *Adv. Opt. Mater.* **2015**, 3, 618; b) D. J. Kim, T. Y. Jeon, S. G. Park, H. J. Han, S. H. Im, D. H. Kim, S. H. Kim, *Small* **2017**, 13, 1603971; c) S. Shin, J. Lee, S. Lee, H. Kim, J. Seo, D. Kim, J. Hong, S. Lee, T. Lee, *Small* **2017**, 13, 1602865.
- [5] a) I. J. Jahn, O. Zulkovskaja, X. S. Zheng, K. Weber, T. W. Bocklitz, D. Cialla-May, J. Popp, *Analyst* **2017**, 142, 1022; b) H. Wang, Y.-L. Zhang, W. Wang, H. Ding, H.-B. Sun, *Laser Photonics Rev.* **2017**, 11, 1700212.
- [6] a) Z. Zhu, Q. Wu, S. Han, W. Xu, F. Zhong, S. Yuan, P. Dwivedi, T. Si, R. X. Xu, *Sens. Actuators, B* **2018**, 275, 190; b) Z. Zhu, T. Si, R. X. Xu, *Lab Chip* **2015**, 15, 646; c) Z. Zhu, Q. Wu, G. Li, S. Han, T. Si, R. X. Xu, *J. Mater. Chem. B* **2016**, 4, 2723.
- [7] a) D. Ji, A. Cheney, N. Zhang, H. Song, J. Gao, X. Zeng, H. Hu, S. Jiang, Z. Yu, Q. Gan, *Adv. Opt. Mater.* **2017**, 5, 1600592; b) B. Song, Y. Yao, R. E. Groenewald, Y. Wang, H. Liu, Y. Wang, Y. Li, F. Liu, S. B. Cronin, A. M. Schwartzberg, S. Cabrini, S. Haas, W. Wu, *ACS Nano* **2017**, 11, 5836; c) F. Liu, B. Song, G. Su, O. Liang, P. Zhan, H. Wang, W. Wu, Y. Xie, Z. Wang, *Small* **2018**, 14, 1801146.
- [8] R. Takahashi, T. Fukuoka, Y. Utsumi, A. Yamaguchi, *Jpn. J. Appl. Phys.* **2013**, 52, 06GK12.
- [9] a) D. B. Litt, M. R. Jones, M. Hentschel, Y. Wang, S. Yang, H. D. Ha, X. Zhang, A. P. Alivisatos, *Nano Lett.* **2018**, 18, 859; b) Z. Lao, Y. Hu, C. Zhang, L. Yang, J. Li, J. Chu, D. Wu, *ACS Nano* **2015**, 9, 12060; c) Z. X. Lao, Y. L. Hu, D. Pan, R. Y. Wang, C. C. Zhang, J. C. Ni, B. Xu, J. W. Li, D. Wu, J. R. Chu, *Small* **2017**, 13, 1603957.
- [10] a) M. De Volder, A. J. Hart, *Angew. Chem., Int. Ed.* **2013**, 52, 2412; b) J. H. Cho, M. D. Keung, N. Verellen, L. Lagae, V. V. Moshchalkov, P. Van Dorpe, D. H. Gracias, *Small* **2011**, 7, 1943; c) S. Lee, B. Park, J. S. Kim, T. I. Kim, *Nanotechnology* **2016**, 27, 474001; d) C. Zhu, G. Meng, P. Zheng, Q. Huang, Z. Li, X. Hu, X. Wang, Z. Huang, F. Li, N. Wu, *Adv. Mater.* **2016**, 28, 4871; e) R. A. Hughes, E. Mennerov, S. Neretina, *Nanotechnology* **2017**, 28, 282002; f) X. Wang, S. G. Park, J. Ko, X. Xiao, V. Giannini, S. A. Maier, D. H. Kim, J. Choo, *Small* **2018**, 14, 1801623; g) K. Wu, T. Li, M. S. Schmidt, T. Rindzevicius, A. Boisen, S. Ndoni, *Adv. Funct. Mater.* **2018**, 28, 1805738; h) H. G. Duan, K. K. Berggren, *Nano Lett.* **2010**, 10, 3710; i) S. M. Kim, J. Kim, S. M. Kang, S. Jang, D. Kang, S. E. Moon, H. N. Kim, H. Yoon, *Small* **2016**, 12, 3764.
- [11] G. Perozziello, R. Catalano, M. Francardi, E. Rondanina, F. Pardeo, F. D. Angelis, N. Malara, P. Candeloro, G. Morrone, E. D. Fabrizio, *Microelectron. Eng.* **2013**, 111, 314.
- [12] B. B. Xu, Z. C. Ma, H. Wang, X. Q. Liu, Y. L. Zhang, X. L. Zhang, R. Zhang, H. B. Jiang, H. B. Sun, *Electrophoresis* **2011**, 32, 3378.
- [13] W. Wu, L. Liu, Z. Dai, J. Liu, S. Yang, L. Zhou, X. Xiao, C. Jiang, V. A. Roy, *Sci. Rep.* **2015**, 5, 10208.
- [14] a) B. B. Xu, R. Zhang, X. Q. Liu, H. Wang, Y. L. Zhang, H. B. Jiang, L. Wang, Z. C. Ma, J. F. Ku, F. S. Xiao, H. B. Sun, *Chem. Commun.* **2012**, 48, 1680; b) S. Bai, D. Serien, A. Hu, K. Sugioka, *Adv. Funct. Mater.* **2018**, 28, 1706262.

- [15] a) Y. J. Oh, K. H. Jeong, *Adv. Mater.* **2012**, *24*, 2234; b) H. Y. Chen, M. H. Lin, C. Y. Wang, Y. M. Chang, S. Gwo, *J. Am. Chem. Soc.* **2015**, *137*, 13698; c) C. Kim, S. Baek, Y. Ryu, Y. Kim, D. Shin, C. W. Lee, W. Park, A. M. Urbas, G. Kang, K. Kim, *Sci. Rep.* **2018**, *8*, 15144.
- [16] a) M. Li, F. Zhao, J. Zeng, J. Qi, J. Lu, W.-C. Shih, *J. Biomed. Opt.* **2014**, *19*, 111611; b) H. Mao, W. Wu, D. She, G. Sun, P. Lv, J. Xu, *Small* **2014**, *10*, 127; c) J. Leem, H. W. Kang, S. H. Ko, H. J. Sung, *Nanoscale* **2014**, *6*, 2895.
- [17] Z.-C. Ma, Y.-L. Zhang, B. Han, X.-Q. Liu, H.-Z. Zhang, Q.-D. Chen, H.-B. Sun, *Adv. Mater. Technol.* **2017**, *2*, 1600270.
- [18] a) Z. Gan, Y. Cao, R. A. Evans, M. Gu, *Nat. Commun.* **2013**, *4*, 2061; b) L. R. Meza, S. Das, J. R. Greer, *Science* **2014**, *345*, 1322.
- [19] a) J. C. Ni, Z. Y. Wang, Z. Q. Li, Z. X. Lao, Y. L. Hu, S. Y. Ji, B. Xu, C. C. Zhang, J. W. Li, D. Wu, J. R. Chu, *Adv. Funct. Mater.* **2017**, *27*, 1701939; b) Z. Lao, D. Pan, H. Yuan, J. Ni, S. Ji, W. Zhu, Y. Hu, J. Li, D. Wu, J. Chu, *ACS Nano* **2018**, *12*, 10142.
- [20] a) M. Hu, F. S. Ou, W. Wu, I. Naumov, X. Li, A. M. Bratkovsky, R. S. Williams, Z. Li, *J. Am. Chem. Soc.* **2010**, *132*, 12820; b) F. S. Ou, M. Hu, I. Naumov, A. Kim, W. Wu, A. M. Bratkovsky, X. Li, R. S. Williams, Z. Li, *Nano Lett.* **2011**, *11*, 2538; c) S.-G. Park, C. Mun, X. Xiao, A. Braun, S. Kim, V. Giannini, S. A. Maier, D.-H. Kim, *Adv. Funct. Mater.* **2017**, *27*, 1703376.
- [21] J. Mosafer, M. Teymouri, *Artif. Cells, Nanomed., Biotechnol.* **2018**, *46*, 1146.